

False Alarm Reduction in Wavelength–Resolution SAR Change Detection Schemes by Using a Convolutional Neural Network

Alexandre Becker Campos[✉], *Member, IEEE*, Mats I. Pettersson[✉], *Member, IEEE*,
Viet Thuy Vu[✉], *Senior Member, IEEE*, and Renato Machado[✉], *Member, IEEE*

Abstract—In this letter, we propose a method to reduce the number of false alarms in a wavelength–resolution synthetic aperture radar (SAR) change detection scheme by using a convolutional neural network (CNN). The detection is performed in two steps: change analysis and object classification. A simple technique for wavelength–resolution SAR change detection is implemented to extract potential targets from the image of interest. A CNN is then used for classifying the change map detections as either a target or nontarget, further reducing the false alarm rate (FAR). The scheme is tested for the CARABAS-II data set, where only three false alarms over a testing area of 96 km² are reported while still sustaining a probability of detection above 96%. We also show that the network can still reduce the FAR even when the flight heading of the SAR system measurement campaign differs by up to 100° between the images used for training and test.

Index Terms—CARABAS-II, change detection, convolutional neural network (CNN), synthetic aperture radar (SAR), target detection.

I. INTRODUCTION

THE use of multitemporal synthetic aperture radar (SAR) images, i.e., SAR images acquired in the same geographical area but at different time instants, has provided solutions for a wide range of remote sensing applications, such as climate monitoring and deforestation control. Their use can also be expanded for target detection: the image background can be suppressed by comparing SAR images from different flight passes, and the targets can be located considering a change detection analysis. In this scenario, the main challenge is to provide a rate of false alarms per square kilometer low enough to be useful to the operator [1].

Manuscript received May 15, 2020; revised August 9, 2020 and September 9, 2020; accepted October 20, 2020. This work was supported in part by the Brazilian National Council for Scientific and Technological Development (CNPq) and in part by the Brazilian Coordination for the Improvement of Higher Education Personnel (CAPES). (*Corresponding author: Alexandre Becker Campos.*)

Alexandre Becker Campos is with the Aeronautics Institute of Technology (ITA), São José dos Campos 12228-900, Brazil, and also with the Blekinge Institute of Technology (BTH), 371 79 Karlskrona, Sweden (e-mail: beckercampos@ieee.org).

Mats I. Pettersson and Viet Thuy Vu are with the Blekinge Institute of Technology (BTH), 371 79 Karlskrona, Sweden.

Renato Machado is with the Aeronautics Institute of Technology (ITA), São José dos Campos 12228-900, Brazil.

Color versions of one or more of the figures in this letter are available online at <https://ieeexplore.ieee.org>.

Digital Object Identifier 10.1109/LGRS.2020.3034758

Low-frequency SAR systems that operate in the very-high-frequency (VHF) or ultrahigh-frequency (UHF) band with large fractional bandwidths provide the required stability for an efficient change detection analysis [2]. The scattering process of wavelength–resolution SAR systems is only related to scatterers with dimensions in the order of the signal wavelengths, which can severely reduce speckle noise. Moreover, low-frequency wavelength–resolution SAR suffers less attenuation due to foliage than more commonly used band SAR systems. Hence, VHF-band systems can be especially suitable for foliage penetration (FOPEN) applications, such as the detection of vehicle-sized targets concealed by foliage. In [1], a set of 24 VHF ultrawideband (UWB) wavelength–resolution SAR images was made publicly available as part of the CARABAS-II data set. The imaged area, located in northern Sweden, is the same for all available images, and 25 vehicles are distributed within each one of them. For this data set, there are four possible target deployments and three different imaging geometries. For each deployment, the target’s location and orientation change. Hence, a change detection analysis can be made to identify the position of targets within a test image.

The stability of the clutter and noise of the CARABAS-II images supports simple but efficient change detection methods that operate on a pixel-by-pixel basis [3]–[5]. Such methods, however, can still be affected by noise fluctuations over two multitemporal images. Furthermore, elongated structures reported within the imaged area are considered to be the main source of false alarms [6]. Two main approaches for overcoming this problem can be identified: the use of image stacks [6], [7] and supervised algorithms [8]. In [9], a combination of both approaches is introduced. The stacks approach employs more than one reference image to reduce the influence of noise and structures related to the background. Supervised algorithms acquire empirical-based knowledge about the targets by performing training based on sliding windows that comprise not only each pixel under test but also their neighborhood.

We propose the use of convolutional neural networks (CNNs) for change discrimination. Given the unique stability of low-frequency wavelength–resolution SAR images, the task of discerning large objects from military vehicles can be seen as a mostly geometry-based problem. CNNs can excel in this situation, as their feature extraction process is primarily based on extracting visual features from the images. This capability has been shown extensively for object classification in optical images, and their application in SAR

images have been expanded for both change detection [10] and object classification [11] in SAR systems using higher frequency bands. Their use for wavelength–resolution SAR change detection, however, is yet to be explored.

In this letter, we introduce the use of a CNN as a filter to reduce the occurrence of false alarms in wavelength–resolution SAR change detection. The proposed target detection scheme differentiates from the previous works as we perform a double detection. First, an initial change map (CM) is generated to detect differences between two multitemporal SAR images on a pixel-by-pixel basis. Second, the detections based on the initial CM are grouped to form larger objects and then are reassessed by a CNN to reduce the number of false alarms. We show that the proposed end-to-end target detection scheme achieves the lowest number of false alarms ever reported for the CARABAS-II data set. Furthermore, we investigate the capability of CNNs to reject false alarms in CARABAS-II images with different flight headings.

The remainder of this letter is organized as follows. Section II describes the proposed target detection scheme. Section III provides the results for the CARABAS-II data set. Finally, Section IV summarizes the conclusions.

II. PROPOSED SCHEME

Let us consider two geo-coded and coregistered magnitude SAR images, \mathbf{I}_r and \mathbf{I}_s , both of size $H \times W$ and acquired in the same geographical area but at two different time instants. The first acts as the background representation and, therefore, is called a reference image. We aim to identify the targets that appear in the latter, i.e., the surveillance image.

We divided the target detection problem into three parts (see Fig. 1).

- 1) *Change Map*: A CM that highlights differences between the reference and surveillance images is generated.
- 2) *Object Extraction*: Windows surrounding each group of connected pixels (objects) of the CM are extracted.
- 3) *Object Classification*: A classification technique to assign each object of the CM as either a target or nontarget is employed, in which the objects classified as nontarget are discarded. The output is a binary image that contains only objects associated with targets from the surveillance image.

A. Change Map

A simple CM for UWB wavelength–resolution SAR images may be obtained through a difference image, thresholding, and morphological operations. We first use a pixelwise subtraction [6]–[8] to obtain a difference image

$$\mathbf{I}_d = \mathbf{I}_s - \mathbf{I}_r. \quad (1)$$

A binary image \mathbf{I}_λ is then obtained by thresholding the entire change image with a single threshold λ

$$\mathbf{I}_\lambda = \mathbf{I}_d > \lambda, \quad \lambda = \mu_d + \alpha \times \sigma_d \quad (2)$$

where μ_d and σ_d are the mean and standard deviation of \mathbf{I}_d , respectively, and α is the detection constant showing how strict

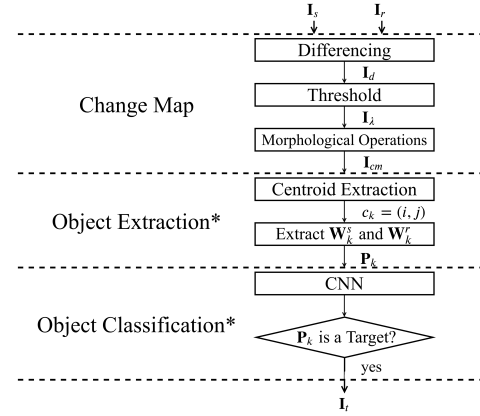


Fig. 1. Proposed scheme for target detection. The superscript “*” indicates that the step is repeated until every object detected in \mathbf{I}_{cm} is tested.

is the thresholding. The higher the α , the lower the number of detected objects tends to be. The pixels with amplitudes below the threshold are set to zero, and the remaining ones will be subject to morphological operations. We employ the morphological operations of opening and dilation with the same structuring element \mathbf{S}_e . The structuring element is linked to the spatial resolution of the system and is defined once for the considered data set so that the objects smaller than it will be removed, while the objects separated by less than this distance can be locally connected, forming larger structures. Thus, the output after the morphological operations is a binary image with the mathematical representation given by

$$\mathbf{I}_{cm} = (\mathbf{I}_\lambda \circ \mathbf{S}_e) \oplus \mathbf{S}_e \quad (3)$$

where \circ and \oplus stand for the morphological operations of opening and dilation, respectively.

B. Object Extraction

The binary image \mathbf{I}_{cm} can be seen as a set of objects distributed within the same geographical region of the reference and surveillance images. Therefore, for each object, we extract their centroid coordinates $c_k = (i, j)$, and consider a block $h \times h$, centered in c_k , as the region of interest related to this object. Given that the amplitude information of both the reference and surveillance images is available, we extract windows \mathbf{W}_k^s and \mathbf{W}_k^r in a way that $\mathbf{W}_k^s = \{\mathbf{I}_s(x, y) | i - \lceil h/2 \rceil + 1 \leq x \leq i + h - \lceil h/2 \rceil, j - \lceil h/2 \rceil + 1 \leq y \leq j + h - \lceil h/2 \rceil\}$, and $\mathbf{W}_k^r = \{\mathbf{I}_r(x, y) | i - \lceil h/2 \rceil + 1 \leq x \leq i + h - \lceil h/2 \rceil, j - \lceil h/2 \rceil + 1 \leq y \leq j + h - \lceil h/2 \rceil\}$, where $\lceil \cdot \rceil$ denotes a round toward positive infinity. Therefore, \mathbf{W}_k^s and \mathbf{W}_k^r are windows that contain the amplitude information of \mathbf{I}_s and \mathbf{I}_r , respectively, associated with a geographical location of size $h \times h$, centered in c_k (when h is odd). Each object within \mathbf{I}_{cm} has a sample \mathbf{P}_k associated with it, composed of both \mathbf{W}_k^s and \mathbf{W}_k^r windows side by side, forming an $h \times 2h$ structure. An example illustrating this is shown in Fig. 2.

C. Object Classification

Each object within \mathbf{I}_{cm} can be classified as either a target or a nontarget structure. We define this as a binary classification problem. Let $\Omega = \{\omega_t, \omega_n\}$ be the set of classes to be

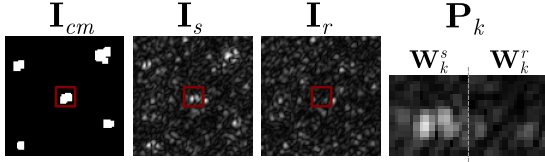


Fig. 2. Illustration of sample extraction. Given a CM \mathbf{I}_{cm} , for each object (bright connected pixels), a block $h \times h$ (highlighted within the images) is extracted for both \mathbf{I}_s and \mathbf{I}_r . A sample \mathbf{P}_k of size $h \times 2h$ is formed by merging \mathbf{W}_k^s and \mathbf{W}_k^r side by side. The sample \mathbf{P}_k was zoomed, and a dashed line was included for better visualization of the windows.

TABLE I
DESCRIPTION OF THE IMPLEMENTED CNN ARCHITECTURE

Layer	Dimension	Activation
Input (\mathbf{P}_k)	$16 \times 32 \times 01$	
Convolutional	$16 \times 32 \times 10$	ReLU
Max-Pooling	$08 \times 16 \times 10$	
Convolutional	$08 \times 16 \times 20$	ReLU
Max-Pooling	$04 \times 08 \times 20$	
Fully connected	640	ReLU
Output	2	

identified, where, for each sample \mathbf{P}_k , we need to decide if it corresponds to a target ω_t or a nontarget ω_n class. For this problem, supervised schemes for the CARABAS-II challenge have attempted to manually craft features based on the local statistics of the samples [8], which are not designed to capture edges and basic shapes that may better discriminate targets from the false alarms. We propose to use a CNN for this task.

The first layer of a CNN extracts features, such as edges and the samples' geometry, and as the number of layers increases, high-level features are extracted. This is particularly useful for the CARABAS-II problem, as the geometry can be very important when it comes to distinguishing elongated structures from military vehicles. We propose a simple architecture composed of two convolutional and two max-pooling layers given the low speckle noise and stability of the considered images, as the use of fewer layers can prevent a massive loss of spatial context from the samples. The architecture parameters for the proposed network are shown in Table I.

The inputs of the CNN are the samples \mathbf{P}_k , of size 16×32 , as we selected $h = 16$. Each convolutional layer, activated by a rectified linear unit (ReLU) function, uses filters whose sizes are 3×3 , while the max-pooling layer reduces the feature map of the previous layer by a factor of two. A fully connected layer generates 640 features used to classify the inputs into two classes, either a target or a nontarget.

III. EXPERIMENTAL RESULTS

For the experiments, we considered the CARABAS-II data set, composed of 24 VHF UWB SAR images related to the same region in Sweden, and acquired at three different flight headings. Each image has a size of 3000×2000 pixels associated with an area of six square kilometers, and each image pixel represents 1 m in azimuth and 1 m in range. The spatial resolution in this measurement campaign is 2.5 m in

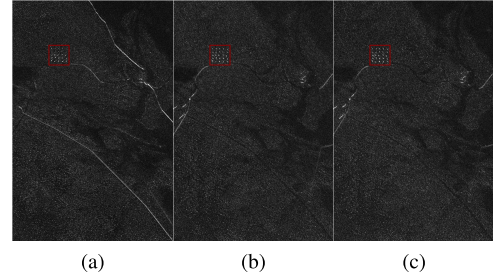


Fig. 3. Images related to the Sigismund deployment, with the 25 targets highlighted within the red square. (a) Image 2_2, flight heading of 135° . (b) Image 2_1, flight heading of 225° . (c) Image 2_5, flight heading of 230° .

azimuth and range [1], [3], and therefore, we use a 3×3 matrix as the structuring element \mathbf{S}_e for (3). Each image of the data set has 25 concealed targets that are arranged in four possible target deployments: Sigismund, Karl, Fredrik, and Adolf-Fredrik. Each target deployment is associated with a specific target placement within the image and a specific target heading. There are three possible vehicle classes: TGB11, TGB30, and TGB40. While the last two are similar in size, the first one is considerably smaller. For the scope of this letter, we will consider that all vehicles belong to the same target class. The images can play the role of \mathbf{I}_r and \mathbf{I}_s for a total number of 24 pairs, as suggested in [1]. Fig. 3 shows the resulting images for the three possible flight headings of the same deployment. The images collected with the flight headings of 225° and 230° are the most affected by radio frequency interference (RFI) since the antenna main lobe is pointing toward a TV transmitter located southeast of the test area [1].

In this letter, we define two databases for training: T_1 , which considers all three flight headings and the four target deployments to achieve a robust classifier; T_2 , to evaluate the performance of the proposed scheme when training with a very different flight heading (135°) than those from the remaining pairs (225° and 230°). The information about the 24 pairs is presented in Table II. Note that, for both T_1 and T_2 , we do not train the algorithm on pairs 18 and 20. These two specific pairs have been reported as the most challenging ones for this data set as their images are highly affected by RFI [4]–[6], and therefore, the number of false alarms tends to be higher. We choose these pairs as part of the test database to evaluate the proposed scheme's performance against this problem.

The training of the network proceeds as follows. For each image pair \mathbf{I}_s and \mathbf{I}_r of the training set, the CM and object extraction steps from Sections II-A and II-B are applied. As the target's location for each pair is available, samples related to objects extracted within a radius of ten pixels from those regions will be assigned as part of the ω_t class. Common false alarms, i.e., noisy pixels and the elongated structures not related to targets, will be detected by the CM and automatically assigned to the ω_n class.

For both training and test, a value of $\alpha = 2$ for (2) was adopted for the CM step as it was capable of reporting the targets while still reducing the algorithm's search space from 6×10^6 pixels to a few hundred objects to be tested per pair. For the CNN displayed in Table I, a standard stochastic

TABLE II
INFORMATION ABOUT THE CARABAS-II DATA SET PAIRS, DATABASE SELECTION, AND DETECTION
RESULTS FOR BOTH THE PROPOSED METHODOLOGIES

Pair	Image (Mission_Pass [1])		Deployment (I_s)	Flight Heading	Database		N_{dt}		N_{fa}	
	I_s	I_r			T_1	T_2	T_1	T_2	T_1	T_2
01	2_1	3_1	Sigismund	225°	Test	Test	25	25	0	0
02	3_1	4_1	Karl	225°	Train	Test	–	25	–	4
03	4_1	5_1	Fredrik	225°	Test	Test	25	25	0	0
04	5_1	2_1	Adolf-Fredrik	225°	Train	Test	–	25	–	3
05	2_2	4_2	Sigismund	135°	Train	Train	–	–	–	–
06	3_2	5_2	Karl	135°	Train	Train	–	–	–	–
07	4_2	2_2	Fredrik	135°	Train	Train	–	–	–	–
08	5_2	3_2	Adolf-Fredrik	135°	Test	Train	22	–	0	–
09	2_3	5_3	Sigismund	225°	Test	Test	24	24	1	2
10	3_3	2_3	Karl	225°	Test	Test	22	22	0	0
11	4_3	3_3	Fredrik	225°	Test	Test	25	25	1	3
12	5_3	4_3	Adolf-Fredrik	225°	Test	Test	25	25	0	1
13	2_4	3_4	Sigismund	135°	Test	Train	25	–	0	–
14	3_4	4_4	Karl	135°	Test	Train	25	–	0	–
15	4_4	5_4	Fredrik	135°	Test	Train	25	–	0	–
16	5_4	2_4	Adolf-Fredrik	135°	Train	Train	–	–	–	–
17	2_5	4_5	Sigismund	230°	Train	Test	–	25	–	1
18	3_5	5_5	Karl	230°	Test	Test	19	21	1	3
19	4_5	2_5	Fredrik	230°	Train	Test	–	24	–	0
20	5_5	3_5	Adolf-Fredrik	230°	Test	Test	24	23	0	2
21	2_6	5_6	Sigismund	230°	Test	Test	25	25	0	1
22	3_6	2_6	Karl	230°	Test	Test	24	25	0	0
23	4_6	3_6	Fredrik	230°	Test	Test	25	25	0	0
24	5_6	4_6	Adolf-Fredrik	230°	Test	Test	25	25	0	0

gradient descent with momentum (SGDM) optimizer was employed, with 15% of the training data used for validation. For the sample size, values of h in a range of 14 to 20 were used, with $h = 16$ providing the best detection result.

To evaluate the proposed approach, the following metrics were used. The probability of detection (P_d) is the sum of detected targets N_{dt} over the available number of targets N_{gt} . Since we are considering 16 test pairs per experiment, $N_{gt} = 400$. The most important metric for radar target detection is the false alarm rate (FAR), which is the total number of detected false alarms N_{fa} over square kilometer covered by the test images, equivalent to an area of 96 km². We also propose to use the figure-of-merit (FoM) metric, as it can be seen as a relationship between the P_d and FAR metrics. It is given by $FoM = N_{dt}/(N_{fa} + N_{gt})$. The higher the FoM, the better the detection performance is.

A. Classification and CM Analysis

We first demonstrate the effectiveness of the CNN for reassessing the CM detections. In Table III, we show the total number of objects detected within the CMs of all test pairs. These detections can be divided into the corresponding amount of detected targets N_{dt} and false alarms N_{fa} for the CM and for the proposed framework (CM + CNN). The amount of N_{dt} and N_{fa} directly correlates to the number of true positives and false positives, respectively. If only the CM is employed, all the detections will be assigned as targets, and therefore, the number of false alarms will be high. This highlights the importance of a detection classification step in this situation.

From Table III, it is possible to infer the capability of the CNN for rejecting the false alarms detected in the CM. Even for the T_2 methodology, where the flight heading changes a lot between the network training and test, the CNN is still

TABLE III
CLASSIFICATION RESULTS FOR THE CM ONLY AND WHEN
THE CNN IS USED WITH THE CM (CM + CNN)

Methodology	Detections	CM		CM + CNN	
		N_{dt}	N_{fa}	N_{dt}	N_{fa}
T_1	3377	399	2978	385	3
T_2	3164	399	2765	389	20

able to report a high number of targets with the cost of a slightly increased number of false alarms. In addition, as only the objects reported by the CM will be processed by the CNN, the CM approach has the benefit of reducing the number of samples to be processed. If a pixel-by-pixel classification was applied, for each set of test pairs, 96×10^6 samples would be tested. For the proposed approach, this number is reduced to about 3000 samples. This is a direct consequence of the value set for the thresholding constant α : the higher the α , the lower the number of detections is, and consequently, a greater reduction in the algorithm's search space is achieved. However, if α is set too high, the samples related to targets will be discarded before the CNN classification step.

B. Detection Results and Flight Heading Sensibility

In Tables IV and V, we compare our proposal with target detection schemes already proposed for the CARABAS-II data set: the space-time adaptive processing (STAP) approach of [3], the statistical hypothesis tests (SHTs) based on the bivariate Gamma [5] and Gaussian distributions [7], the I-RELIEF approach of [9], and the logistic regression presented in [8]. Note that, as we only evaluate the model for the test pairs, we display the results shown in [3], [5], and [7]–[9] for the same 16 pairs of each methodology. For

TABLE IV

COMPARISON BETWEEN THE PROPOSED MODEL WITH THE T₁ METHODOLOGY AND OTHER TARGET DETECTION SCHEMES

Algorithm	P_d	FAR	FoM
STAP [3]	0.9600	0.7604	0.8118
Bivariate Gamma SHT [5]	0.9575	0.4479	0.8645
Bivariate Gaussian SHT [7]	0.9550	0.1458	0.9227
Logistic Regression [8]	0.9525	0.2812	0.8923
I-RELIEF [9]	0.9675	0.1667	0.9303
CM	0.9975	31.021	0.1181
CM + ResNet-18	0.9725	0.0313	0.9653
CM + CNN	0.9625	0.0313	0.9553

TABLE V

COMPARISON BETWEEN THE PROPOSED MODEL WITH THE T₂ METHODOLOGY AND OTHER TARGET DETECTION SCHEMES

Algorithm	P_d	FAR	FoM
STAP [3]	0.9500	0.7292	0.8085
Bivariate Gamma SHT [5]	0.9575	0.5000	0.8549
Bivariate Gaussian SHT [7]	0.9550	0.2396	0.9031
Logistic Regression [8]	0.9500	0.3646	0.8736
I-RELIEF [9]	0.9750	0.2187	0.9264
CM	0.9975	28.802	0.1261
CM + ResNet-18	0.9025	0.2083	0.8595
CM + CNN	0.9725	0.2083	0.9262

our proposed model, we used the CNN of Table I (CM + CNN) and a fine-tuned deep residual network with 18 layers based on [12] (CM + ResNet-18) as the object classifier.

Table IV shows that the proposed algorithm achieves the lowest FAR reported for the CARABAS-II data set with a P_d above 96% for both classifiers and also surpasses all the other target detection schemes by at least 2% in FoM. It is important to note that the approaches presented in [7] and [9] used two and three reference images, respectively. For the proposed algorithm, we used a single reference image, the same as in [3], [5], and [8].

In Table V, we analyze our classification results when only images acquired with the 135° flight heading were used for training. Note that, as we do not retrain the supervised approaches of [8], [9] for this case, their results are still reproduced in this letter as a result of their original training procedure. The proposed model is still capable of overcoming the target detection schemes based only on two images of [3], [5], and [8] and performs better than the stacks approach of [7]. The results are similar to the approach of [9], which uses three reference images and employs preprocessing and postprocessing. This result highlights the capability of the proposed CNN to learn the targets' structure even if the flight heading is changed drastically, as a high correlation between targets is still expected. A loss in performance for the ResNet-18 classifier is noticeable and indicates that a greater generalization can be achieved with the proposed CNN. A higher number of false alarms are reported as the elongated structures related to the false alarms are more sensitive to the flight path (see Fig. 3), and therefore, the objects that will be detected by the CM will change considerably. In addition, as the test images of this experiment are considered to be the most affected by RFI, the results indicate that the scheme is robust against this problem.

IV. CONCLUSION

In this letter, we presented a twofold solution to the problem of detecting targets for wavelength-resolution multitemporal SAR images. First, we generate a CM to highlight objects within the images employing a simple thresholding technique. Second, after extracting samples related to the objects, we use a CNN to distinguish targets from other strong scatterers detected in the CM to further reduce the FAR. The simple proposed scheme overcame the performance of statistical tests, other supervised algorithms, and even the schemes that make use of more than one reference image. This is particularly visible for pair 18 of the CARABAS-II data set, where only one false alarm is reported for the most challenging image pair of the available data. In addition, we explored the network learning capability when images acquired with a single flight heading are used for training, and as the experiment achieved decent results, we conclude that the proposed scheme can still be applicable in those conditions. The combination of change analysis and a classification algorithm for multitemporal SAR images target detection can be explored further, as the proposed CM step can be replaced with other suitable techniques. A stricter CM step can be investigated and could imply a simpler object classification step, as the target detection scheme can now be seen as a combination of two algorithms.

REFERENCES

- [1] M. Lundberg, L. M. H. Ulander, W. Pierson, and A. Gustavsson, "A challenge problem for detection of targets in foliage," *Proc. SPIE*, vol. 6237, May 2006, Art. no. 62370K.
- [2] R. Machado, V. T. Vu, M. I. Pettersson, P. Dammert, and H. Hellsten, "The stability of UWB low-frequency SAR images," *IEEE Geosci. Remote Sens. Lett.*, vol. 13, no. 8, pp. 1114–1118, Aug. 2016.
- [3] L. M. H. Ulander, M. Lundberg, W. Pierson, and A. Gustavsson, "Change detection for low-frequency SAR ground surveillance," *IEE Proc.-Radar, Sonar Navigat.*, vol. 152, no. 6, pp. 413–420, Dec. 2005.
- [4] N. R. Gomes, P. Dammert, M. I. Pettersson, V. T. Vu, and H. Hellsten, "Comparison of the Rayleigh and K-Distributions for application in incoherent change detection," *IEEE Geosci. Remote Sens. Lett.*, vol. 16, no. 5, pp. 756–760, May 2019.
- [5] V. T. Vu, N. R. Gomes, M. I. Pettersson, P. Dammert, and H. Hellsten, "Bivariate gamma distribution for wavelength-resolution SAR change detection," *IEEE Trans. Geosci. Remote Sens.*, vol. 57, no. 1, pp. 473–481, Jan. 2019.
- [6] V. T. Vu, M. I. Pettersson, R. Machado, P. Dammert, and H. Hellsten, "False alarm reduction in wavelength-resolution SAR change detection using adaptive noise canceler," *IEEE Trans. Geosci. Remote Sens.*, vol. 55, no. 1, pp. 591–599, Jan. 2017.
- [7] V. T. Vu, "Wavelength-resolution SAR incoherent change detection based on image stack," *IEEE Geosci. Remote Sens. Lett.*, vol. 14, no. 7, pp. 1012–1016, Jul. 2017.
- [8] R. D. Molin, R. A. S. Rosa, F. M. Bayer, M. I. Pettersson, and R. Machado, "A change detection algorithm for SAR images based on logistic regression," in *Proc. IEEE Int. Geosci. Remote Sens. Symp. (IGARSS)*, Jul. 2019, pp. 1514–1517.
- [9] W. Ye, C. Paulson, and D. Wu, "Target detection for very high-frequency synthetic aperture radar ground surveillance," *IET Comput. Vis.*, vol. 6, no. 2, pp. 101–110, Mar. 2012.
- [10] F. Gao, X. Wang, Y. Gao, J. Dong, and S. Wang, "Sea ice change detection in SAR images based on convolutional-wavelet neural networks," *IEEE Geosci. Remote Sens. Lett.*, vol. 16, no. 8, pp. 1240–1244, Aug. 2019.
- [11] C. Bentes, D. Velotto, and B. Tings, "Ship classification in TerraSAR-X images with convolutional neural networks," *IEEE J. Ocean. Eng.*, vol. 43, no. 1, pp. 258–266, Jan. 2018.
- [12] K. He, X. Zhang, S. Ren, and J. Sun, "Deep residual learning for image recognition," in *Proc. IEEE Conf. Comput. Vis. Pattern Recognit. (CVPR)*, Jun. 2016, pp. 770–778.